



Research paper

Spatio-temporal analysis of scour around complex offshore foundations under clear water and live bed conditions

Mario Welzel^{a,*}, Alexander Schendel^a, Ramish Satari^b, Insa Neuweiler^b, Torsten Schlurmann^a

^a Ludwig-Franzius-Institute for Hydraulic, Estuarine and Coastal Engineering, Leibniz University of Hannover, Germany

^b Institute of Fluid Mechanics and Environmental Physics in Civil Engineering, Leibniz University of Hannover, Germany

ARTICLE INFO

Keywords:

Scour
Jacket
Laboratory tests
Sediment transport
Erosion patterns

ABSTRACT

This study investigates scour around offshore wind foundations, focusing on two complex structures with varying degrees of flow blockage: a novel hybrid gravity-based jacket (structure “A”) and a conventional four-legged jacket (structure “B”). As offshore structures like jackets become more prevalent, mainly due to their structural stability and growth of offshore wind energy in general, understanding scouring phenomena around complex structures is crucial. Laboratory tests under steady flow clear-water and live-bed conditions, with measurements of 3D laser scans for test durations of 15, 90, and 420 min were conducted. In addition the scour development over time was measured and analyzed with eight echo sounders. The findings confirm that scouring around complex structures displays significant variability in dependency of the structure type, making standardization a challenging task. However, some common trends can be derived. Under live-bed conditions, both types of structures exhibit global erosion, regardless of the complexity or flow obstruction of the structure. The spatial erosion depth, relative to the footprint, is markedly higher (2.5 times) for the gravity-based structure as opposed to the jacket structure. In clear-water conditions, no global scour was observed for both structures and a very similar spatial erosion depth was reached after 420 min.

1. Introduction

Despite the significant acceleration in the expansion of the offshore wind sector in recent decades (WindEurope, 2021), substantial growth is still needed to meet the renewable energy targets set by the European Union to achieve climate neutrality by 2050. Offshore wind energy expansion sites are highly contested, requiring careful consideration of demands from several stakeholders. To enhance energy generation and efficiency, these sites are progressively developed and located farther from the coastline and in deeper waters (WindEurope, 2021). In these conditions, complex foundation structures such as jackets offer an improved structural stability at a lower cost than monopiles, which is essential for future mega-structures with hub heights exceeding 200 m. As a result, the share of installed jacket structures in Europe is increasing. Jacket structures are in Europe the second most prevalent type of substructures (9.9%, 568) after monopiles (81.2%) (WindEurope, 2021). Fig. 1 shows a sketch of common offshore wind foundation substructures. In addition to jacket structures, gravity-based structures comprise a total of 289 installed substructures, while tripods account for

126 and tripiles for 80 in Europe (data from 2020; WindEurope, 2021). Due to varying environmental conditions (e.g. typhoon or earthquake), offshore wind substructures are subject to different structural requirements in dependency of the individual location. For example, in some regions of Asia, there is a growing trend of using jacket structures and high-rise pile cap foundations (Xiao et al., 2021).

One of the major threats to the stability of offshore foundation structures is the development of scour. While considerable research has been conducted on the pointwise equilibrium scour depth around monopile foundation structures in the past (e.g. Melville and Coleman, 2000; Sumer and Fredsøe, 2001, 2002; Schendel et al., 2020), there is only a limited number of studies focusing on the scour development around more complex substructures. The scouring process around complex offshore structures is different from that around cylindrical structures such as monopiles due to the superposition of local scour, and global erosion processes. These differences are highly dependent on the specific structural geometry. These complex foundation structures can lead to significant spatial morphological alterations and substantial sediment displacement, potentially impacting the structural stability

* Corresponding author.

E-mail addresses: welzel@lufi.uni-hannover.de (M. Welzel), schendel@lufi.uni-hannover.de (A. Schendel), satari@hydromech.uni-hannover.de (R. Satari), neuweiler@hydromech.uni-hannover.de (I. Neuweiler), schlurmann@lufi.uni-hannover.de (T. Schlurmann).

<https://doi.org/10.1016/j.oceaneng.2024.117042>

Received 20 November 2023; Received in revised form 20 January 2024; Accepted 4 February 2024

Available online 22 February 2024

0029-8018/© 2024 The Authors. Published by Elsevier Ltd. This is an open access article under the CC BY license (<http://creativecommons.org/licenses/by/4.0/>).

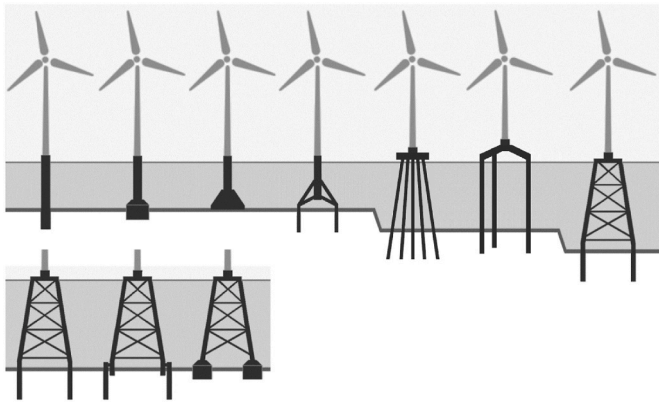


Fig. 1. Sketch of common bottom fixed offshore wind foundation structure types. From left to right: monopile, suction bucket monopile, gravity-based, tripod, high-rise pile cap, tripod with pre pile, jacket with post pile, jacket with suction bucket.

and marine ecosystems. Knowledge of scour around monopiles is therefore of limited use for design purposes, as depths and patterns can vary considerably. The interactions of flow and combinations of structural elements have been studied using pile groups. A better understanding could help to transfer knowledge about scour around pile groups to more complex structures as complex offshore structures often include or consist of a specific arrangement of piles as presented and discussed in detail in Welzel (2021).

A better understanding of the interference effects between a group of two piles is thus fundamental.

For close spacings $G/D < 2$, the flow around piles in tandem arrangement act as a “single body”. At intermediate spacings of $2 < G/D < 5$, vortices are formed on the lee side of the upstream pile which reattach on the downstream pile. Larger pile spacings of $G/D > 5$ allow for a free vortex interaction between both piles (Sumner, 2010). The flow around two piles in side-by-side arrangement with $0 < G/D < 0.1-0.2$ behaves as the flow around a single body. If the gap between the piles increases $0.1-0.2 < G/D < 1-1.2$, the flow in the gap is biased due to an asymmetrical vortex pattern. If the gap increases further $G/D > 1-1.5$ both piles exhibit independent behavior of the flow with unbiased vortex shedding (Sumner, 2010). The scour development at pile groups is directly influenced by the aforementioned flow regimes and spacings between the piles. In addition the scour development is also affected by a change in the flow pattern based on the eroded or deposited sediment behind or in front of each pile, which occurs due to an overlapping of scour holes in close proximity (Beg, 2008; Hosseini and Amini, 2015).

Various studies focusing on groups of circular cylinders have analyzed the dependency between the distance between piles (gap ratio) and the dynamics of scour development, both for local and global scour development under current conditions (Sumer et al., 2005; Amini et al., 2012; Hosseini and Amini, 2015). Another example of scour at complex structures under the influence of currents are complex bridge piers. As an example Ghodsi et al. (2021) experimentally investigated local scour depth around complex bridge piers in clear-water conditions in eighty-two experiments using six model types. However, the number of studies with a hexagonal cylinder arrangement is rather limited, as presented in the following. Yagci et al. (2017) have studied the scour development around a hexagonal array of 7 circular cylinders for three orientations (regular, angled and staggered) and different gap ratios between the cylinders. They measured scour depths of approximately $S/D = 2-3$ (S : scour depth; D : diameter) with maximum values of up to $S/D = \sim 4$ after test durations of 8 h. As one result, the measurements show clearly deeper scour depths for the staggered orientation (90° rotation) as for the regular orientation (0° rotation), while the angled orientation (15° rotation) reveals larger scour depths as the staggered

orientation for gap to pile diameter ratios $G/D \leq 0.85$ and smaller scour depths for $G/D \geq 1.44$. Ni and Xue (2020) studied five different foundation types, including a tripod and hexapod foundation as well as a triangular pile group consisting of four and a hexagonal array consisting of seven circular cylinders. Ni and Xue (2020) measured maximum scour depth end values of S/D of about 2.2–2.8 for the hexapod foundation, as well as maximum scour depths of $S/D = 2.1-2.4$ for hexagonal arrays of seven cylinders. The scour development was measured via a camera system over a time period of 30 h. In addition, the authors compared the accuracy of three equilibrium scour depth prediction equations, for which the FDOT method by Sheppard and Miller, 2006) provided the best results, with comparable accurate and conservative predictions.

Bolle et al. (2012) and Baelus et al. (2019) studied scour depth field measurements at a jacket structure (with D approx. = 2 m) in the Thornton Bank offshore wind farm, southern North Sea. The authors analyzed several multi-beam surveys of the scour pattern, recorded at various intervals across a time period of three years. Baelus et al. (2019) measured maximum scour depths of approximate $S/D = 0.78-0.98$ (1.55–1.95 m). Chen et al. (2023) investigated the scour development around a jacket structure under current only clear-water conditions over a time period of up to 40 h in a laboratory. The authors observed a linear relation between the maximum scour depth and the flow strength and water depth. Furthermore, they also observed a strong influence in form of a reduced scour depth on the rear piles, despite of tests with an inclined orientation of the jacket, as the rear piles are directly affected and have a reduced shielding effect for an inclined orientation.

Welzel et al. (2019a, 2019b) conducted experimental laboratory tests and developed prediction equations to estimate the local and global scour at a generic jacket structure. The structural impact on the scour development was found to be most pronounced around the main piles in the vicinity of the diagonal braces. In consequence, Welzel et al. (2020) conducted additional tests, investigating the structural influence of the lowest node and diagonal braces on the scour development and refined the prediction equation estimating the scour development around jacket structures. Besides the vertical position of the lowest node, the structural diameter, the existence and diameter of horizontal and or diagonal braces as well as the foundation type (pre or post-pile foundation) is significant for the scour development at jacket structures. The scour development at a jacket structure with diagonal and horizontal braces and a post pile foundation is presented in Rudolph et al. (2004). The study reveals a large global scour, along with a local scour at the main piles that was 3–4 times larger than that estimated for a single pile. This magnitude of scour depth differs from the findings of Welzel et al. (2019a,b). Considering the results of Welzel et al. (2020), it is assumed that the large local scour development reported by Rudolph et al. (2004) is mainly due to the additional influence of the post pile foundation. For additional literature, the authors refer to Welzel et al. (2019a,b), who reviewed existing works pertaining to scour development around jacket structures.

The growing utilization of complex foundation structures, coupled with a lack of systematic studies and limited understanding of the hydrodynamics and scour around these structures, raises concerns about their structural safety, cost effectiveness and environmental impact. This is particularly relevant for novel designs of foundation structures, such as the hybrid gravity-based jacket foundation studied herein, whose ongoing development is being driven by the expansion of offshore wind energy. This particular structure combines a six-legged jacket design with a gravity foundation that incorporates suction bucket foundations.

Investigating the influence of the geometric features of this structure, the paper compares it to a 4-legged jacket structure. The 4-legged jacket is also selected, as it represents the counterpart, an offshore structure with a hydrodynamically transparent design, as the ratio of obstructed to total flow cross-section is relatively small in comparison to the six-legged jacket. On the other hand, the gravity-based hybrid structure has a significant larger structural surface area, resulting in a higher ratio of obstructed area compared to the flow cross-section.

The hybrid structure's design is undoubtedly unique. Transferring the findings on scour development to alternative structures will present challenges. However, the comparison of both foundation structures enhances the understanding of the structure-current-sediment interactions around complex structures and helps to evaluate the impact of varying levels of flow obstruction on the scour process. The findings can raise awareness among designers of novel offshore foundation structures of the issue of hydrodynamic transparency and the resulting effects on the scour process. In contrast to the increasing popularity of complex offshore structures in response to increasing water depths and loads (WindEurope, 2021), the literature and understanding of scour at such structures remains limited, as also shown and remarked in Welzel (2021). To the best of the authors knowledge, studies regarding the temporal scour development and spatial analysis of topographic changes around jacket structures on these length scales have been published even more rarely. As discussed in Welzel et al. (2019a,b), previously utilized (Bolle et al., 2012) approaches regarding scour development at monopiles and scour at pile groups (Breusers, 1972; Hirai and Kuruta, 1982; Sumer et al., 2005) are not sufficient to predict the complex scour processes at jacket structures and their influence of additional diagonal, horizontal struts and other structural elements. Studies on more complex bridge piers also differ greatly from complex offshore structures, both structurally and in terms of their loading and water depth.

Thus the present study also aims to contribute as a valuable source to estimate temporal scour depths, spatial scour patterns and erosion volumes at offshore jacket structures under current load.

The present study is based on Welzel et al. (2023) and extends the study aiming to evaluate the influence of flow blockage (hydrodynamic transparency) on the scour process around complex offshore structures by exemplarily comparing an unconventional, hydrodynamic compact structure with a more hydrodynamic transparent jacket structure. The main objectives are:

- High resolution measurement of the spatio-temporal evolution of the scour process with 3D-Scans at different time periods under current load.
- Quantification of spatio-temporal scour development around a conventional jacket and a six-legged gravity-based jacket foundation with a significantly increased flow blockage.
- Assessment of the influence of the structural geometry and flow blockage of complex foundations on the spatial scour development with the dimensionless erosion depth.
- Analysis and comparison of the scour development over time for a conventional jacket structure with low blockage and the six-legged jacket structure with a high flow blockage at eight locations, including reference positions, influenced by global erosion.

2. Experimental setup & procedure

Physical model tests were carried out at the Ludwig-Franzius-Institute, Leibniz University of Hannover, Germany, using a state-of-the-art 3D wave current basin. The basin is 40 m long and 24 m wide and allows for water depths up to about 1 m. A sediment deepening section is located in the center of the basin, spanning 8 m in length and 6.6 m in width, while offering an extended depth of 1.2 m. To prevent significant recirculation of sediment carried by the flow as bedload, a sediment trap is located downstream of the sediment pit. A unidirectional current is generated by a pumping system of four pumps, achieving a maximum combined flow rate of 5 m³/s, which corresponds to a depth-averaged mean flow velocity of up to 0.5 m/s at a water depth of 0.6 m. The structure alignment in reference to the current direction was kept constant during the model tests and can be observed in Fig. 2, a. A water level of 0.67 m was kept constant during the whole test program with both structure types (assuming a model length scale of 1:45, this corresponds to a prototype water depth of 30 m). As large parts of the experimental setup and procedure are identical to that described

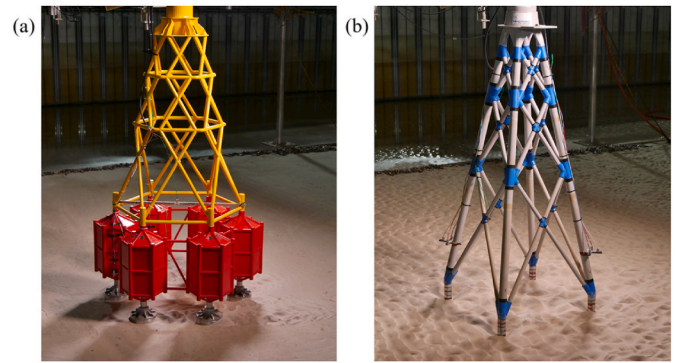


Fig. 2. (a) Photo of the 6-legged jacket gravity foundation structure “structure A” (b) photo of the conventional 4-legged jacket structure “structure B”. Both in the sediment pit of the wave basin of the Ludwig-Franzius-Institute.

in Welzel et al. (2019a,b, 2020), this chapter describes only the essential parts of the experimental setup. More detailed information about the facility, the setup and the conventional 4-legged jacket structure can be found in Welzel et al. (2019b, 2020). To ensure comparability, both sets of tests – one with the unconventional gravity-based jacket structure and the other with the more commonly used 4-legged jacket structure – followed the same procedure and setup. Matching hydrodynamic boundary conditions, model scale, and general instrumentation were applied. The gravity-based jacket substructure (original design concept: Maritime Offshore Group) consists of six legs with a large container at each leg. Each of the six legs has two diagonal braces attached to it. These twelve diagonal braces are joined at a horizontal strut, which is repeated three times up to the top of the transition piece (see Fig. 2, a). The lower containers served a dual purpose: offering buoyancy for the jacket during transportation to the installation site and providing support during the installation process through continuous filling with sand or stones. This, in turn, increased the overall structural stability due to the added weight. However, these containers do not sit directly on the seabed. Instead, they are positioned at a distance of about 10 cm above the seabed. Furthermore, to enhance the stability, the jacket is connected to the seabed using suction buckets. The model of the 6-legged novel gravity-based (Fig. 2, a) and the conventional 4-legged jacket (Fig. 2, b) foundation structures were 3D-printed in stiff plastic in multiple parts, which were connected, glued together and finished with filler and varnish. The finish with filler and subsequently with varnish smoothed the surface and strengthened the connections of the overall structure. For simplicity, we will refer to the unique 6-legged gravity-based foundation structure from now on as “structure A”, and the conventional 4-legged jacket structure as “structure B” (see also Fig. 2, a).

The six suction buckets for structure A were fabricated from steel, incorporating a deep embedment into the sediment and a rigid connection to the flume bottom. As a preparation of each test, the sediment surface was flattened with aluminum bars, at a level, that the top of the suction buckets were positioned 3 cm above the sediment bed. A schematic sketch as well as dimensions of structure A and B is given in Fig. 3. Sand with a median diameter of $d_{50} = 0.19$ mm, a geometric standard deviation of $\sigma_s = \sqrt{d_{84}/d_{16}} = 1.4$ and a density of $\rho_s = 2.65$ g/cm³ was utilized. The grain size distribution of the utilized sediment is additionally displayed in Appendix A. A high-resolution terrestrial 3D laser scanner (Focus 3D, Faro, Lake Mary, FL, USA) was utilized to measure scour and erosion patterns of the sediment surface. The 3D laser scanner is a suitable measuring instrument for surveying high-resolution terrain models (with up to 70 million data points per scan, at a grid resolution of 1 mm). In the present laboratory application, the 3D laser scanner allowed a higher resolution than comparable methods (photogrammetry, echo sounders, etc.), which allows a detailed analysis of the erosion patterns and sediment transport volumes around the small and

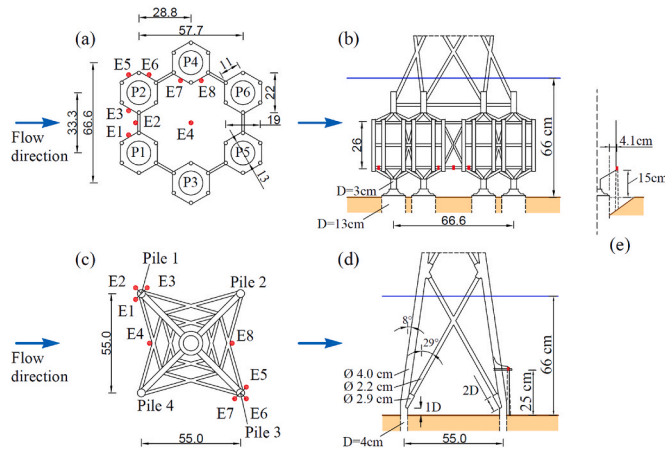


Fig. 3. Schematic view on structure A and B, including dimensions and water depth: (a) plan view (b) side view on structure A (6-legged gravity foundation structure), including the structural reference diameter $D = 13$ cm (c) plan view (d) side view on structure B (4-legged jacket), including the structural reference diameter $D = 4$ cm and (e) detail of echo sounder at structure A.

complex structures (structure B, $D = 4$ cm). To ensure spatial reference for each measured scan, six reference spheres were used as preparation for the laser scan measurements in each test. To avoid shadowing, six scans were performed for each experiment at different positions in the wave basin, which were subsequently merged with the program FARO® SCENE. In the further processing steps, data outliers of the laser scans were reduced using the CloudCompare software. The pre-processed data were then imported into matlab for further processing.

Current induced flow velocities were measured using an Acoustic Doppler Velocimeter (ADV) (Vectrino+, Nortek AS, Norway), positioned 2.5 m upstream of the structure model. The ADV has been positioned 10 cm above the sediment bed. The undisturbed current velocity close to the sediment bed is referred to as U_c , while the depth averaged current velocity is referred to \bar{U} , which was processed with a vertical profile measurement of the undisturbed current velocity. Due to ripple migration and sediment transport close to the sediment bed, a reliable flow measurement below 10 cm was not possible. Eight small echo sounding sensors (E1-E8, Ultrasonic Ranging System – URS, Seatek), 1 cm in diameter each, were positioned for each test series around structure A and structure B to enable monitoring the temporal evolution of scour in the vicinity of the complex structures (see Fig. 3).

Due to the small size of the sensors, a respective distant from the sensor to the sediment bed and the capabilities of the sensor system to measure high resolution bed changes under high sediment transport rates, a nearly non-intrusive measurement of the scour development over time could be achieved at these complex structures. A similar echo sounding system was utilized by McGovern et al. (2014) as well as Gong et al. (2023).

Echo sounders (URS) at structure A were positioned around pile 1, 2 and 4 as well as in the center of the structure. The sensors E1, E3 and E5-E8 have been mounted at the surface of the hexagonal containers in a horizontal distance of 4.1 cm to the pile wall and a vertical offset of 15 cm (see Fig. 3e). Echo sounder sensor E2 is positioned in-between pile 1 and pile 2, while sensor E4 is positioned in the center of the structure. The echo sounder sensors (URS) were installed at structure B (4-legged jacket structure) in a distance of 1 cm to the main piles to ensure that the sound footprints were positioned directly close to the pile (half beam angle of the URS = 0.9°). Measurements of the URS have been collected in a resolution of 1 mm. All sensors were installed at a distance of 25 cm from the flat bed (~ 6 diameters of the main piles of structure B), ensuring a compromise between a comparable small footprint of 2 cm as well as a distance to the sediment bed, which is far enough to abate the intrusiveness of the artificial structure of the sensor. Similar as described

in Welzel et al. (2019a,b), adjustments related to water temperature, density, threshold voltage, along with reference measurements in calm conditions and diverse signal filters were taken into account to guarantee a high quality of the scour development measurements. In the instrumentation for the 4-legged jacket, structure B, 6 sensors were installed around the main piles, pile 1 (E1, E2 and E3) and pile 3 (E5, E6 and E7) (see Figure, 3), while one (sensor E4) were installed in between Pile 1 and Pile 4 on the upstream side and another one on the downstream side between pile 2 and pile 3 (sensor E8). For further information regarding the echo sounder setup we refer to Welzel et al. (2019a,b) as the instrumentation were similar and described in more detail. The structure orientation of structure A (6-legged gravity foundation structure) was chosen in consideration to investigate the maximum scour development. A similar structure orientation as used in the present study (Fig. 3 a) was investigated in Yagci et al. (2017) for different hexagonal arrays of vertical cylinders, which revealed larger scour depths as a 90° rotated orientation.

2.1. Experimental procedure and test conditions

To prevent sediment settlement during the tests, the sand was placed in wet condition and subjected to several pre-tests to ensure optimum compaction. In addition, glued gravel mats in combination with a geotextile were laid along the inner edge of the 8.0×6.6 m sediment pit, effectively minimizing the scour at the edges. To ensure controlled uniform compaction of the sediment and minimize entrapped air, the sand was installed in wet condition. In addition, several preliminary tests were carried out before the actual test program was started, which also reduced entrapped air and presumably led to a more even compaction. In preparation for each test, the sand was leveled with aluminum bars, while attention was paid to ensure that the close proximity of the structure was not directly loaded during flattening of the sand. This ensured uniform starting conditions, to maintain a consistently smoothed bed level throughout the whole experimental program. Prior to each test, the smoothed bed was scanned after levelling the sediment and the water was slowly let into the wave basin overnight.

Two separate test series were conducted, each for one structure (model A and B). To enable high quality spatio-temporal measurements of the complex bed topography change over time, 12 tests have been conducted in total to adequately capture the temporal change of the bed topography for live bed and clear water current conditions. Three tests have been conducted under a depth averaged velocity of $\bar{U} = 0.42$ m/s, representing live bed conditions, each for structure A (Test 1a – 1c) and B (Test 2a – 2c), see Table 1. Additional three tests were performed for structure A (Test 3a – 3c) and B (4a – 4c) with a flow velocity of $\bar{U} = 0.24$ m/s, representing clear water conditions, see Table 1.

The spatial scour pattern was measured after each test. Each sub test has been conducted as a separate test. The test procedure is explained in the following:

1. Levelling of the sediment bed and 3D laser pre-scan of the smoothed topography prior to the test.
2. Carefully filling in the basin overnight.
3. Conducting the subtest, e.g. test 1a.
4. Emptying the basin overnight and slowly draining the sediment pit at the next day to avoid any influences on the scour pattern.
5. Measuring the bed topography with the 3D laser scanner after test 1a as the post-scan and start again with point (1) for test 1b.

The test duration of subtests c (see Table 1, 420 min) was selected based on previous experiences regarding the equilibrium state of the scour process under similar conditions, where 220 min were mostly sufficient (Welzel et al., 2019a). Additionally, the duration enables the completion of one subtest in 2 days. Although this procedure was time consuming, it provided detailed insights into the temporal spatial

Table 1
Test conditions.

Test	Current velocity 10 cm above bed	Depth averaged velocity	Shields Ratio	Flow velocity ratio	Shields Parameter	Test duration	Structural reference diameter	Structure type
	U_c	\bar{U}	θ/θ_{cr}	\bar{U}/U_{crit}	θ		D	
	[m/s]	[m/s]	[-]	[-]	[-]	[min]	[cm]	
1a	0.225	0.24	0.67	0.76	0.033	15	13	A
1b	0.225	0.24	0.67	0.76	0.033	90	13	A
1c	0.225	0.24	0.67	0.76	0.033	420	13	A
2a	0.225	0.24	0.67	0.76	0.033	15	4	B
2b	0.225	0.24	0.67	0.76	0.033	90	4	B
2c	0.225	0.24	0.67	0.76	0.033	420	4	B
3a	0.388	0.42	1.7	1.31	0.084	15	13	A
3b	0.388	0.42	1.7	1.31	0.084	90	13	A
3c	0.388	0.42	1.7	1.31	0.084	420	13	A
4a	0.388	0.42	1.7	1.31	0.084	15	4	B
4b	0.388	0.42	1.7	1.31	0.084	90	4	B
4c	0.388	0.42	1.7	1.31	0.084	420	4	B

* Structure A: 6-legged gravity based jacket structure.

* Structure B: 4-legged conventional jacket structure.

evolution of scour patterns around complex structures. The test durations of subtests a and b (see Table 1, 15 and 90 min) have been chosen to capture the highly dynamic scour development during the initial stages of the scouring process. The topographic data of each pre and post-scan of the present study is uploaded and freely available. The test conditions are summarized in Table 1.

The Shields parameter θ s calculated with the near bed current velocity U_c and was calculated by applying the shear stress approach of Soulsby and Clarke (2005). The critical Shields parameter of $\theta_{cr} = 0.049$, was calculated based on Soulsby (1997). Given a logarithmic velocity profile U_{crit} is determined as $U_{crit} = 0.297$ m/s on the basis of θ_{cr} .

2.2. Calculation of spatial erosion parameters

On the one hand, this study investigates the scour depths over time measured by echosounder sensors and on the other hand the systematic analysis of complex erosion patterns measured with the 3D laser scanner. For the systematic analysis of topographic erosion patterns, an approach that was introduced by Welzel et al. (2019b) and further developed in Welzel et al. (2020) and Welzel (2021) is utilized, which is only briefly explain here for completeness.

Displaced sediment volumes V_i are calculated for specific areas a_i around the offshore structures. Erosion volumes are considered as a displacement of the digital elevation model (DEM) below the reference pre-scan, while deposition volumes are regarded as a displacement of the DEM above the pre-scan. The volume V_i ($V_i = \sum Z_i(a_i) \bullet A_g$), which is in the following denoted as the “displaced net volume” is calculated as the sum of height differences Z_i over an area a_i within the data matrix of the DEM, which are multiplied by the area of a datapoint A_g . The area of a data point in turn depends on the grid size and thus on the resolution. The interrogation area a_i starts from the centre of the analyzed structure up to a certain maximum area that is still analyzed. The value $D_{i,i}$ is utilized in the present study as the main parameter describing the displacement of sediment volume around offshore structures. In the following $D_{i,i}$ will be referred to the “incremental volume depth”, which is a dimensionless parameter obtained by normalizing V_i with the related interrogation area a_i as well as a structural reference length D . Structural elements which directly obstruct the flow are utilized for the normalization. For structure A the length D equals the suction bucket diameter, while for structure B, the length D is equal to the diameter of the main struts.

$$D_{i,i} = \left(\frac{V_i - V_{i-1}}{a_i - a_{i-1}} \right) / D \quad (1)$$

The lower index (V_{i-1}, a_{i-1}) in equation (1) refers to the volume of increasing interrogation areas, while $D_{i,i}$ relates to a relative volume change per surface area of a volume $V_i - V_{i-1}$ (m^3) within adjacent areas $a_i - a_{i-1}$ (m^2), divided by the reference length D . A detailed description of the calculation of $D_{i,i}$ can be found in Appendix B. This normalized representation enables a direct comparison with S/D scour depth values, as well as the quantification of displaced sediment volumes of each area. This parameter in turn can be used to estimate erosion volumes in the field or to predict complex erosion patterns and global scour in general.

Distances within the presented volume analysis (Figs. 6 and 7) are represented as dimensionless values determined by dividing a length in meter by the structure footprint reference distance, such as $0.5 A = 0.275$ m/0.55 m for the 4-legged or $0.5 A = 0.31$ m/0.62 m for the 6-legged jacket structure (see also Fig. 3, for the structure footprint dimensions; $0.62 = (0.66 + 0.57)/2$).

3. Results

3.1. Spatial scour pattern in clear-water conditions

Fig. 4 compares the spatial scour pattern for both structures at 15, 90, and 420 min intervals for clear-water conditions. The scour pattern time sequence of structure A (6-legged jacket gravity foundation) is shown on the left side of Fig. 4.

The large gravity tanks of structure A have a significant blocking effect on the flow. This causes the incoming flow to either divert sideways or pass over and under the buoyancy containers. Given that the distance perpendicular to the current between pile 4 and 2, as well as between pile 3 and 1, is approximately $1.3D$ (0.167 m), a significant flow acceleration is expected. The distance between the piles is still comparably small, thus a flow acceleration due to the large gravity tanks and the distance between the piles is also expected along the centerline. Structure A is expected to have a large influence on the flow pattern, leading to structure induced vortices and significant flow constriction, due to the structural obstruction. Structure B is a more hydrodynamic transparent foundation with significant less structural obstruction. Nevertheless, a slight flow acceleration in between the structure and a constriction at the main piles and below the diagonal braces is expected, influencing the bed topography.

As the piles are comparably large for structure A and the distances between the piles range from $1.3D$ to $2.6D$, the downstream trails easily overlap and reach neighboring piles. As a consequence of the overlapping, a spatial scour pattern forms in the center of structure A after a test duration of 15 min (see Fig. 4a). At the jacket structure (structure B),

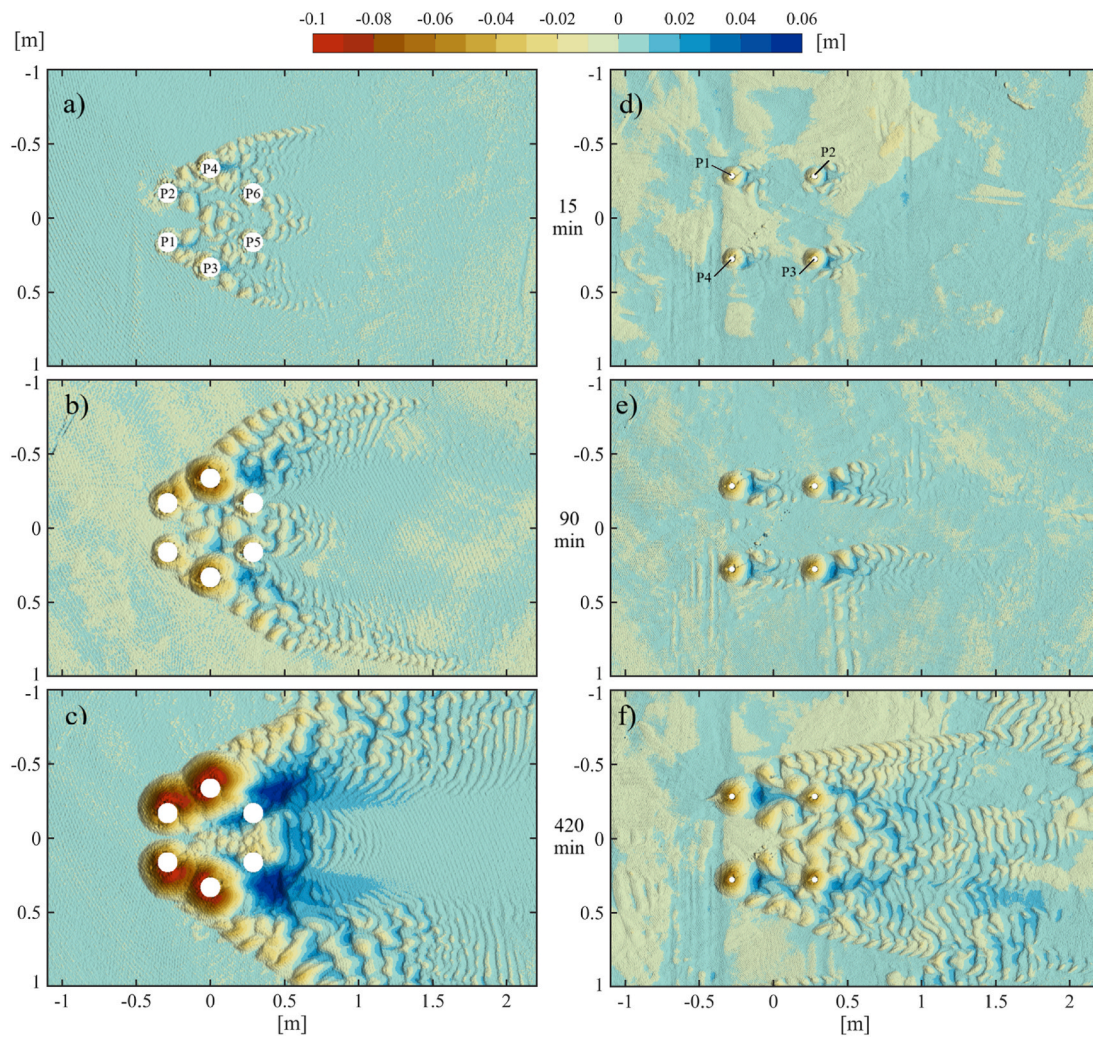


Fig. 4. Scour pattern of test 1, structure A (a) after 15 min loading time, (b) 90 min and (c) 420 min. Scour pattern of test 2, structure B (d) after 15 min, (e) 90 min and (f) 420 min loading time under clear water conditions $U_c = 0.225$ m/s. Current from left to right.

those local scour trails do not overlap after a test duration of 15 min. The scour trails from the upstream piles have not reached the downstream piles. The topographies of both structures (Fig. 4a and d) show individual local scour holes around the piles, after a test duration of 15 min. The depth and extent indicate that the scour development to pile diameter ratio at structure B is progressing faster than at structure A. For clear-water conditions, little influence of other structural elements (e.g. diagonal braces) is apparent in the scour pattern. At this time, no clear global scour is observed for clear-water conditions for both structure types. However, both structure types start to leave distinct downstream trails, induced by velocity peaks of the lee-wake vortices. Despite the shape and extent of the scour development, the laser scans reveal the detailed depths of the scour around the two structures. After a duration of 15 min, the bed topography of structure A exhibited a maximum scour depths of about $0.15D$ (2 cm) at pile 3 and 4 (Fig. 4a), while structure B reveals a maximum scour depth of about $0.5D$ located at the upstream piles 1 and 4 (Fig. 4b).

In case of the 6-legged gravity based structure A, the developing scour pattern distinctly shows an overlap of local scour holes around each pile, after a test duration of 90 min (see Fig. 4b). These downstream scour trails extend and deepen over the time. After 90 min (Fig. 4b), the scour depth around the middle piles 4 and 3 of structure A has reached a value of $0.5D$ (~ 6 – 7 cm). The scour development at the two downstream piles 5 and 6 is clearly influenced by the upstream sediment transport and flow processes resulting from current deflection, scour and sediment

deposition around the upstream and middle piles. This leads to reduced scour depths of around $\sim 0.25D$ (3–3.5 cm) at the downstream piles. In the case of structure B (Fig. 4e), the downstream trails start to reach neighboring piles after 90 min. Extent and depth of scour at the downstream piles is less pronounced than at the upstream piles, indicating an effect of the upstream part of the jacket on the downstream scour process, reaching scour depths of about $1D$ at the upstream piles of the structure B.

After 420 min, the deepest scour of $0.81D$ (10–11 cm) at structure A, developed around the outer side of the middle piles 3 and 4 as well as the outer sides of piles 1 and 2. Thus the scour pattern also indicates that the piles in the middle (pile 3 and 4) are subjected to an increased current velocity due to the former described flow compression. In clear water conditions, structure A's complex geometry results in an equally complex and uneven scour pattern with large local differences in scour depth. The upstream and middle piles show a pronounced scour on the outer sides, while the downstream piles exhibit only slight scour development. In some places, sediment has even accumulated around the two downstream piles. It appears that the downstream piles are shielded from direct current attack. At the same time, the erosion processes on the upstream piles lead to a net sediment influx and deposition around the downstream piles. Deposited sediment in form of downstream trails and ripples due to lee-wake vortices and turbulent mixing lead to a decreased maximum scour depth of $1.43D$ on the downstream side in reference to a scour depth of $1.63D$ on the upstream side of

structure B. From this it is evident that the clear difference between the upstream and downstream scour depth is developing in a later stage of the developing scour hole.

For structure A, the scour apparently does not increase uniformly around all piles. The spatial scour extent around pile 3 and pile 4 of structure A (symmetrical loading), increased from 1.54D (0.20 m; 15min) to 2.46D (0.32 m; 90min), up to 3.46D (0.45 m; 420min) while the scour extent around pile 1 and 2 increased from about 1.31D (0.17 m; 15min) to 2D (0.26 m; 90min), up to 3.15D (0.41 m; 420min) in diameter (see Fig. 4a and b). A reason for the increased scour development at piles 3 and 4 compared to the upstream piles might be flow acceleration between pile 2 and 4 (or 1 and 3, respectively). Furthermore, it is important to mention that the scour shape is not distributed symmetrically around individual piles. For example, at the side of pile 2 towards the center of the structure the scour hole reached an extent of 1.15D (0.15 m) after 420 min. On the outer side of this pile, however, the scour extended to a maximum distance of 2D (0.26 m), which might be explained by the constriction and acceleration of flow in this area. The scour pattern after 420 min of structure B (Fig. 4f) shows that the whole area in between the piles and downstream the offshore structure is captured by downstream trail patterns. At structure B, the scour size expands faster at the upstream than at the downstream piles. At the upstream piles 1 and 4 it expands from 1.1 D after 15 min to 1.9D after 420 min, while at the downstream piles 2 and 3 the extent increases from 1.1 D after 15 min, to 1.5D after 420 min. Thus, we observe an

increase of 72% in the scour extent on the upstream side and an increase of 36% in the extent from 15 min to 420 min on the downstream side.

3.2. Spatial scour pattern in live-bed conditions

Spatial scour patterns in live-bed conditions are shown in Fig. 5 for structure A (Fig. 5a–c) and structure B (Fig. 5d–f). Fig. 5a displays the bed topography after a 15-min test duration under live bed conditions, depicting the scour pattern in an early stage. The flow around the suction buckets of structure A induces local scour at each pile of the foundation. The flow around pile 1 and 2 leads to scour hole extents of approximately 3.3D within the first 15 min. At the middle piles 3 and 4, the scour hole expands to a maximum extent of 3D, while the scour at the downstream piles exhibits an extent of 2.9D at pile 5 and 2.2D at pile 6. After the initial 15 min, there has been no clear global scour development beneath the 6-legged jacket structure, despite the expected acceleration of flow. The maximum scour depths are found on the inner upstream side of each pile (see Fig. 5a), ranging from 0.77D (P3 and P4) to 0.7D (P1,2,5,6). Eroded sediment predominantly accumulates directly at the rear of the structure, 4.3D from the foundation’s center, with a maximum vertical deposition of roughly 0.5D.

Fig. 5b illustrates the scour pattern around the 6-legged jacket structure (structure A) after 90 min test duration. The initially individual scour holes have merged into a singular connecting scour hole, resembling that of a typical scour hole around a pile group. The scour depth in

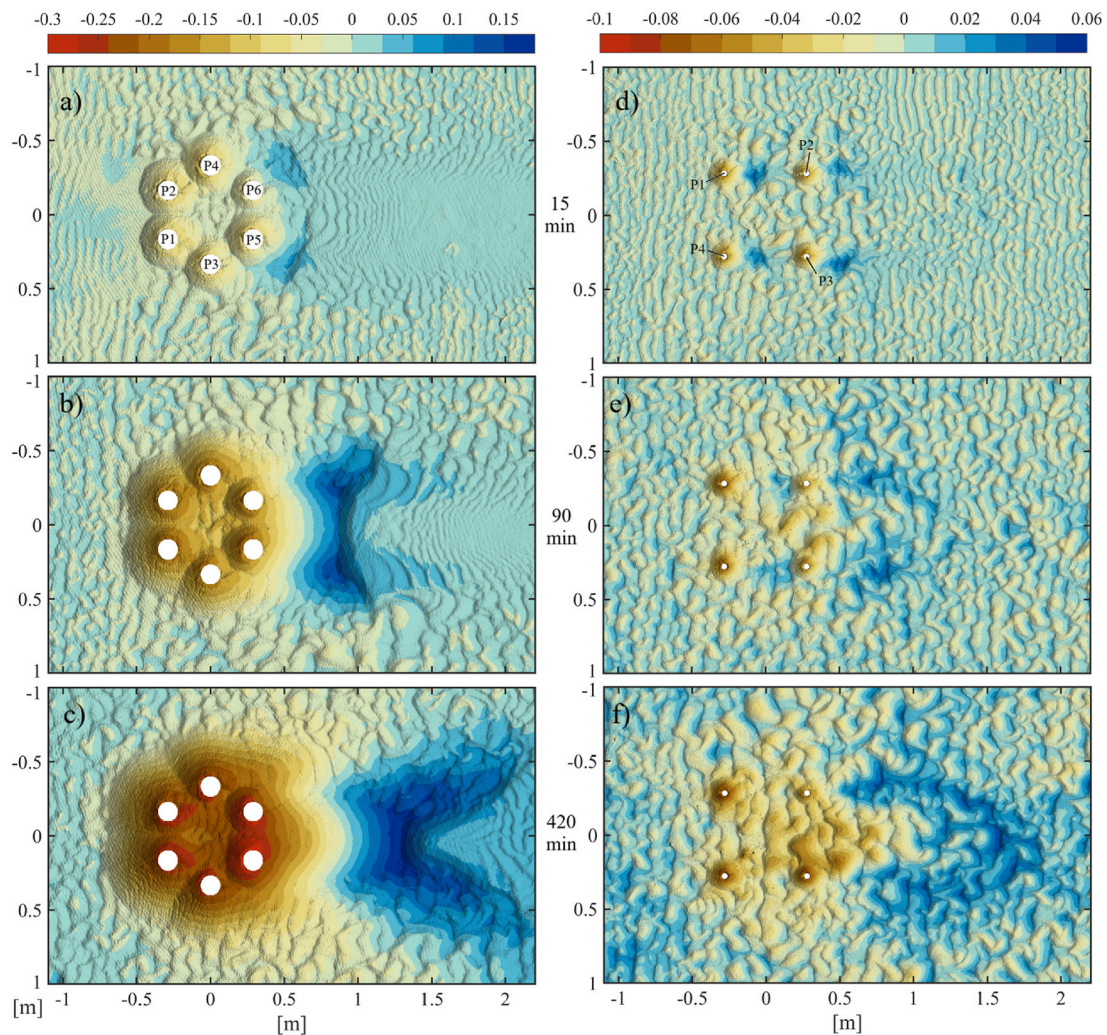


Fig. 5. Scour pattern of test 3, structure A (a) after 15 min loading time, (b) 90 min and (c) 420 min. Scour pattern of test 4, structure B (d) after 15 min, (e) 90 min and (f) 420 min loading time under live-bed conditions $U_c = 0.388$ m/s. Current from left to right.

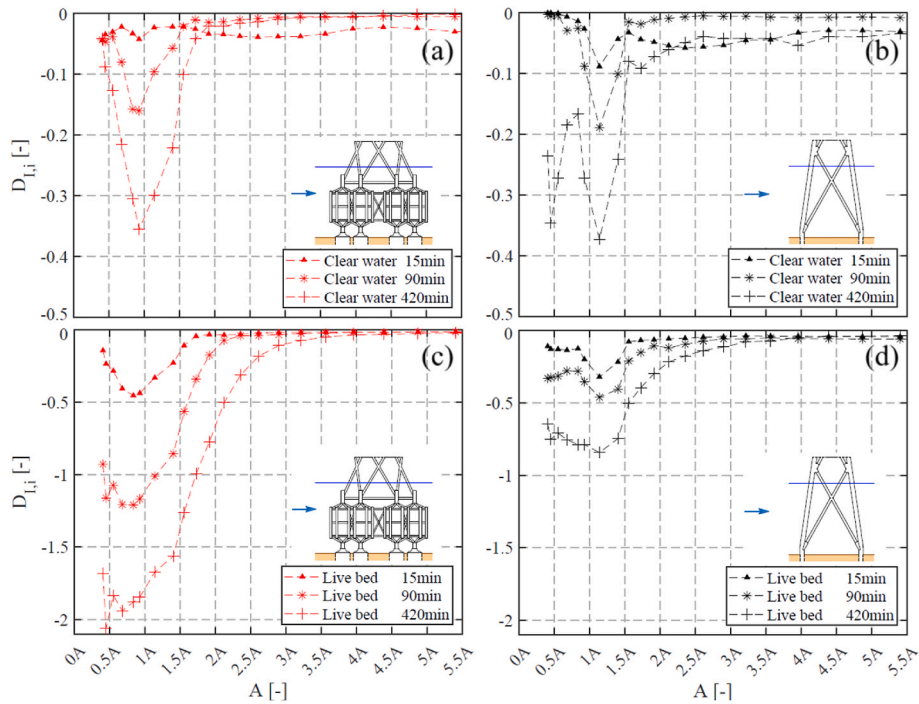


Fig. 6. The incremental volume depth $D_{i,i}$ (Eq. (1)) of eroded sediment as a function of the structure footprint “A” (section 2.2) (a) depicted for Tests 1a – 1c (gravity-base jacket) and (b) for Tests 2a – 2c (4-legged jacket) under clear-water conditions, as well as (c) depicted for Test 3a – 3c and (d) for Test 4a – 4c under live bed conditions.

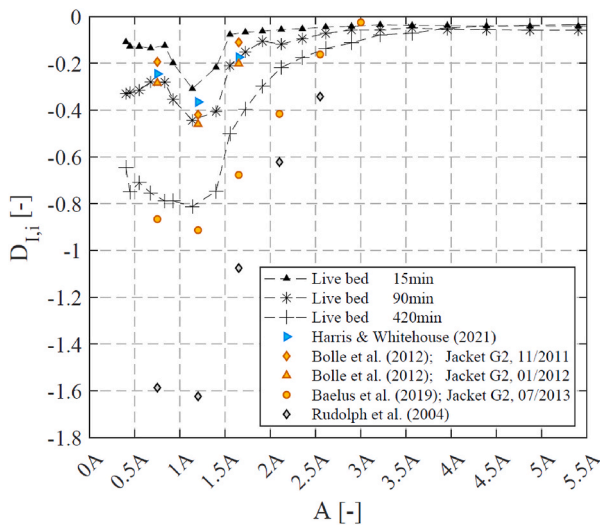


Fig. 7. Incremental volume depth $D_{i,i}$ (Eq. (1)) of eroded sediment as a function of the structure footprint “A” (section 2.2) for Test 4a – 4c under live bed conditions for a common 4-legged jacket, compared with in-situ field measurements of Harris and Whitehouse (2021), Bolle et al. (2012), Baelus et al. (2019) and Rudolph et al. (2004).

the center of the foundation structure remains shallower than directly at the piles. The erosion in the center is affected by the interplay between the individual local scour holes and the assumed flow acceleration beneath and in between the tanks of structure A. Comparing the topography with that observed after 15 min of loading (see Fig. 5a), an increase of approximately 40–50% in scour extent can be noted. This resulted in a merged scour with a diameter of 9.2D (1.2 m). The maximum scour depths are located at each pile on the inner upstream side and are in the range of 1.4D–1.5D, while the scour depth in the center of the structure has increased to about 0.9D. The eroded sediment

is deposited 6.4D from the center in downstream direction with a maximum vertical offset of 1D.

In Fig. 5c, the scour pattern after a test duration of 420 min is shown. The extent of the merged scour hole has increased by additional 17% to 10.8D compared to the topography measured after 90 min. Maximum scour depths are approximately 2D for the upstream and middle piles (P1–P4), while the scour depth at the downstream piles is about 2.3D (P5 and P6) and the erosion depth in the center of the structure is about 1.7D. The deposition peak has shifted downstream, located 9.8D from the center with a maximum vertical deposition offset of 1.3D.

In contrast to the scour development observed in clear-water conditions, the scour pattern surrounding structure B (Fig. 5d–f) displays features of global scour in live-bed conditions. Even after 15 min (Fig. 5d), a slight erosion can be seen below the centre of Structure B, which increases significantly as the test progresses, reaching erosion depths of approximately 1D. Furthermore, significant accumulation downstream of the structure is observed. Compared with the clear-water case, the flow constriction by the structure was large enough to accelerate the flow beneath the structure to a level sufficient to substantially scour the seabed, which was not the case in the clear-water case. Due to the smaller pile diameter and greater distance between piles in comparison to structure A, the local scour holes around structure B have not merged into one as they did in structure A. Compared to the clear water case, the scour pattern around structure A appears to be more evenly distributed as the individual scour holes have partially merged. The deepest scouring was observed around the downstream piles, which experienced negligible scouring under clear water conditions.

Furthermore, the authors refer to Welzel et al. (2019b) for a more detailed description of scour patterns including combined wave-current conditions.

However, there has been a shift in the location of the maximum scour on the upstream and central piles. In clear water conditions, the biggest scour occurred at the outside edge of piles 1–4. In live-bed conditions (Fig. 5c), the maximum scour depth shifted inward towards the inside edge of these piles. Overall, it seems that the strong flow in live-bed conditions is redirected differently than in the clear-water case, so

that flow acceleration below and between the tanks is now dominant. In clear water conditions, the flow was redirected more towards the sides around the tanks.

3.3. Quantification of erosion volumes

Fig. 6 illustrates the spatial distribution of displaced sediment volumes around the foundation structures as dimensionless erosion depth $D_{I,i}$ (see section 2.2 for a description of $D_{I,i}$). Fig. 6a and c shows the erosion for the gravity-base jacket structure, whereas Fig. 6b and d depict the spatial erosion around the 4-legged jacket structure. The distance along the x axis of Fig. 6 is given as a dimensionless value, as an information of distance of an interrogation area divided by the structure footprint reference distance (see chapter 2.2). The incremental erosion depths $D_{I,i}$ are calculated for areas between 0.5 times the footprint of the structure (0.5 A) and 5.5 times the footprint of the structure (5.5 A). The incremental erosion depth $D_{I,i}$ is calculated according to equation (1) and illustrated respectively for the three spatio-temporal measurements for 15, 90 and 420 min loading time.

Fig. 6a and b shows the erosion pattern of test 1 and 2, revealing the spatial scour pattern depicted over time for both investigated structure types under clear-water conditions. A pronounced peak in the normalized erosion depth is observed around ~ 1 A at Fig. 6a, shifting slightly towards smaller A values and 6 b, towards larger values.

The depth and extent of the scour pattern under clear-water conditions, measured after 15 min loading time indicate that the scour development at structure B (Fig. 6b, $-0.09 D_{I,i}$) is progressing faster than at structure A (Fig. 6a, $-0.04 D_{I,i}$). A reason for this might also be to find in the very low height of 1.5 cm of the suction buckets above the bed. This significantly reduces the horseshoe vortex, which at a straight conventional pile contributes significantly to erosion around the pile (add a reference). As the scour around the suction buckets of structure A deepens, the vortex and flow lead over the next time period to a significant increase of the scour depth around each sub pile (Fig. 6a). However, it is important to note that, no global scour was observed and measured under clear-water conditions for both structures over the time span of 420 min. Furthermore it is quite interesting that these offshore structures, which represent remarkable well the extrema of more hydrodynamic transparent (structure B, see Fig. 3) and hydrodynamic compact structures (structure A, see Fig. 3), reveal a very similar normalized erosion pattern, measured after 90 (90min; structure A: max $-0.16 D_{I,i}$; structure B: max $-0.19 D_{I,i}$) and 420 min (420min; structure A: max $-0.36 D_{I,i}$; structure B: max $-0.37 D_{I,i}$) under clear-water conditions (see test 1 and 2, Fig. 6a and b).

Fig. 6c illustrates Test 3, highlighting a peak in maximum erosion intensity between 0.7 and 0.8 A. This peak aligns with the inner zone of the scour hole surrounding the main piles. Excluding the outlier at 0.45 A in Test 3c, we observe a decreasing trend for the normalized erosion intensity in regions smaller than ~ 0.75 A across Tests 3a-3c. This correlates with reduced scour depths at the structure's center illustrated in Fig. 5. Test 3a yielded low erosion rates in the central region of the structure, observed after 15 min.

Due to the degree of flow acceleration as a reason of structural obstruction, a slightly increased spatial erosion beneath the structure was assumed at this point in time (15 min). Increased erosion is noted in the center after 90 and 420 min of loading respectively. This appears due to the overlap of individual scour holes and global erosion, similar to pile group scour (ref). Areas over ~ 0.75 A show comparable decline in tests 3a-3c, likely influenced by the erosion angle of scour holes. Fig. 6d reveals the spatial erosion around a conventional 4-legged jacket structure, tested under identical conditions for tests 1 and 3. The main struts in test 4a-4c have a 4 cm diameter, which is considerable smaller than the 13 cm in test 3a-3c. Fig. 6d compared with 6c therefore highlights the difference in a normalized erosion depth between both structures as a hydrodynamic compact and a hydrodynamic transparent

structure type. The peak erosion depth of test 4a ($-0.3 D_{I,i}$) to 4c ($-0.5 D_{I,i}$) occurs at 1.2 A, around the jacket's 4 main piles.

The 15 min and 90 (test 4a-4b) min scour pattern under live bed conditions of structure B depict greater normalized erosion around the jacket's main piles, see Fig. 6d $\sim 0.8A-1.5$ A, while after 420 min (test 4c) more pronounced global erosion similar to test 3 of structure A (Fig. 6c) is observed. A more even distributed erosion depth in the structure footprint area (from 0 to about 1.2 A), showing the same erosion depth indicates a global scour, while the peak erosion at the piles (around 1 A) clearly decreases if there is no global scour (e.g. see Fig. 6a). Erosion under the 4-legged jacket is likely due to global blockage, approx. ed by the large gap-to-diameter ratio of about 13. However, normalized erosion magnitudes differ significant: test 4c peaks at $-0.8 D_{I,i}$, while the gravity-base jacket, shown in Fig. 6c reaches $-2 D_{I,i}$. A spatio-temporal comparison highlights a faster development of the scour pattern for the gravity-base jacket, which is evident as test 3 b reveals 60% of its final erosion depth ($-1.2 D_{I,i}$) after 90 min, compared to a value of 53% for test 4 b ($-0.45 D_{I,i}$).

Fig. 7 illustrates the dimensionless incremental volume depth $D_{I,i}$ under current only ($\bar{U} = 0.42$ m/s) live bed conditions for the investigated 4-legged jacket model (test 4), depicted over an area of up to 5.5 times the structure footprint at 15 min (test 4a), 90 min (test 4 b) and 420 min (test 4c) loading time. Since the dimensionless parameter $D_{I,i}$ can be directly compared with S/D values of related surfaces, data points of the compared field studies could be determined from topographic surveys (see Appendix B for a detailed description of the calculation). As assessed in chapter 3.4, test 4c reached equilibrium conditions and is thus a good reference for a comparison of in-situ field data of comparable jacket structures. Bolle et al. (2012) and Baelus et al. (2019) illustrated the bed topography of the same jacket structure (pre driven piles $D =$ approx. 2 m, no horizontal braces) over a time period of about three years. The survey 07/2013, presented in Baelus et al. (2019) generally shows a similar spatial distribution and depth as the topography of test 4c, measured after 420 min. Furthermore, the survey captures after 3 and 5 months loading, presented in Bolle et al. (2012) fit remarkably well with the analyzed topography of test 4 b, measured after 90 min. The survey of the bed topography shown in Harris and Whitehouse (2021) shows a scour pattern around a jacket (pre driven piles $D = 1.83$ m, no horizontal braces, jacket main legs 1.52 m), measured one year after installation. A global scour pattern is already visible in the survey of Harris and Whitehouse (2021), which reveals a qualitative resemblance with the general processes studied and data acquired in laboratory and might be, moreover, regarded as quantitatively similar with the spatial extent and depth of test 4 b. The survey shown in Rudolph et al. (2004) on the other hand, reveals a much deeper local and global scour pattern, which might be partly explained as the survey was also taken three years after installation as well as due to the structural design, including horizontal and diagonal braces as well as main piles with $D = 1.1$ m and post piles with $D = 1.2$ m. Thus two piles are obstructing the flow at the sediment water intersection acting as an extended body of one pile for the flow. The scour around the jacket investigated by Rudolph et al. (2004) also revealed local scour depths at the main piles of a factor of 3–4 times the prediction, which can be also explained by the additional post-piles and near bed flow obstruction.

3.4. Time development of scour depth

The applied test duration of 420 min was chosen on the one hand based on experience related to equilibrium conditions with the 4-legged jacket model (Welzel et al., 2019b), and on the other hand due to test-related, practical limitations. An equilibrium scour depth was not reached for all conducted tests. Sheppard et al. (2004, 2006) and Melville and Chiew (1999) conducted tests over long time periods of multiple days, which also showed a correlation between the equilibrium scour depth and the pile diameter. In particular, the clear-water scour

tests of the 6-legged gravity foundation (sediment piercing structural diameter $D = 13$ cm) therefore show the lowest scour depth in relation to the equilibrium scour depth after 420 min of current loading. To estimate equilibrium conditions, an extrapolation was made to determine the expected equilibrium scour depths for each test. A mathematical approach introduced in Welzel et al. (2019b) (Eq. 2) was used to determine a value of 90% of the expected equilibrium scour depths and compared with each scour depth end value S_{end} , similar to Sheppard et al. (2004).

$$S(t) = a \left(1 - \frac{1}{1 + bt} \right) \quad (2)$$

A comparison of Eq. (2), including a and b as fitting parameters, with the mathematical functions of Sheppard et al. (2004) shows that Eq. (2) yields similar equilibrium scour depth values in between both functions of Sheppard et al. (2004), but does a better job of handling irregularities and larger fluctuations in the signal, partly on the downside of a slightly less perfect fit. Comparing 90% of the extrapolated equilibrium scour depths with the measured scour depth S_{end} shows that, except for test 2 at pile 1, reaching only 84% of the predicted equilibrium scour depth (refer to Fig. 9a, E1), measurements at pile 3 during test 2 and test 4 (pile 1 and 3) have achieved an equilibrium condition exceeding 90% of S_{eq} (refer to Fig. 9b–d). The comparison of the measured end scour depths with 90% of the extrapolated equilibrium scour depths of test 1 and test 3, however, shows that the scour requires slightly more time at structure A. Echosounder E1–E4 at test 1 measured only minor scour depths in clear water conditions ($\bar{U} = 0.24$ m/s), which is also related of the echo sounder distance to the pile. Therefore, only the scour development at E6 was assessed (giving a reference for E5–E8), which showed that 71% of the equilibrium scour depth had been reached (see Fig. 9b). Test 3 under live bed conditions, on the other hand, shows a rather uniform scour development in comparison of the eight echo sounders. To give a reference, Echo sounder 1 and 6 has been analyzed (82% of S_{eq} at E1 and

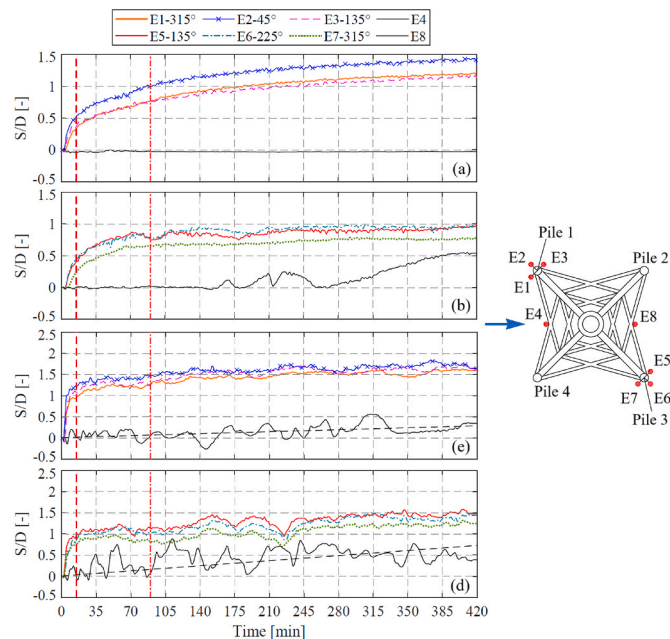


Fig. 8. Scour progression over time for structure B, 4-legged jacket structure; (a) echo sounder E1–E3 at pile 1 and E4, $\bar{U} = 0.24$ m/s (b) echo sounder E5–E7 at pile 3, $\bar{U} = 0.24$ m/s (c) E1–E3 at pile 1 and E4, $\bar{U} = 0.42$ m/s (d) E5–E7 at pile 3, $\bar{U} = 0.42$ m/s; $\bar{U} = 0.24$ m/s = depth averaged current velocity under clear-water conditions; $\bar{U} = 0.42$ m/s live bed conditions; E4 and E8 are positioned to measure the global scour depth on the upstream and downstream side. Dashed black line: linear regression respectively of E4 and E8, starting with $S/D = 0$.

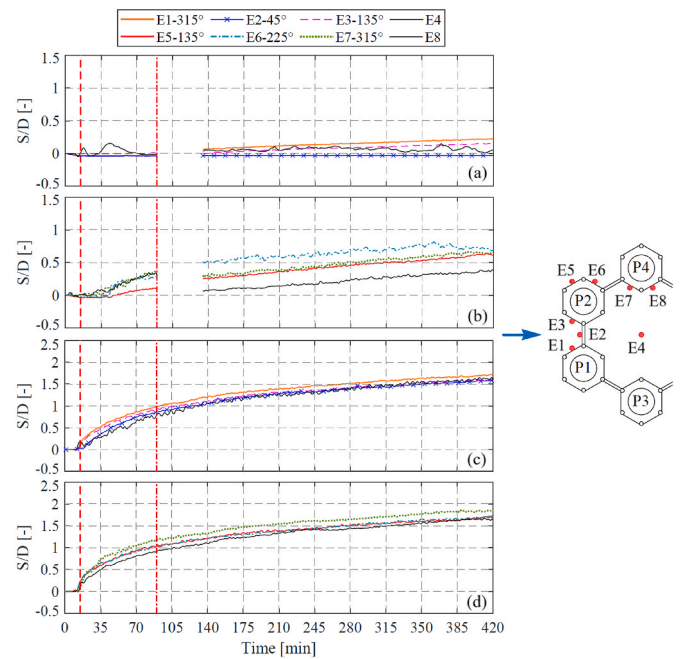


Fig. 9. Scour progression over time for structure A, 6-legged gravity-based foundation structure; (a) echo sounder E1–E4, $\bar{U} = 0.24$ m/s (b) echo sounder E5–E8, $\bar{U} = 0.24$ m/s (c) E1–E4, $\bar{U} = 0.42$ m/s (d) E5–E8, $\bar{U} = 0.42$ m/s; $\bar{U} = 0.24$ m/s = depth averaged current velocity under clear-water conditions; $\bar{U} = 0.42$ m/s live bed conditions; E2 and E4 are positioned in a reference position, E2 in between P1 and P2 on the upstream side and E4 in the center to measure influence on global erosion.

87% at E6, see Fig. 9 c and d).

Utilizing Eq. (2) or the approach of Sheppard et al. (2004) on the global scour development data of test 4 (see Fig. 9c and d) echo sounder E4 and E8 appears to be rather difficult, as a comparison shows that for E4 11% and for E8 80% of the equilibrium scour depth has been reached. As pointed out the global scour (E4 and E8) observed under live bed conditions for structure B appears to be on a different time scale as the local scour development. Therefore, the applied duration of 420 min is not sufficient to be able to make a proper statement about the equilibrium condition of E4 and E8 of test 4.

Based on Figs. 8 and 9, the time development of scour between the two structures is compared in the following. The tests with a duration of 420 min (1–4c) are shown for both the clear-water and the live-bed case. However, due to a failure of the echosounders, the scour data at the start of the clear water test for Structure A, shown in Fig. 9, was lost. To give an idea of the initial scour development in this test, the scour development from the 90-min test has been added. However, this results in some discontinuities in the overall scour development, and therefore the initial scour development in this test is not discussed further in the following analysis. It is also important to note that the scour depth obtained with the echosounder are not directly comparable. In case of structure B, the 4-legged jacket, scour measurements with the echosounder were done very close to the main piles. For structure A, the hybrid gravity-based structure, scour depths were recorded below the outer edge of the ballast tanks, and thereby in a distance of about 3–4 cm from the suction buckets. Therefore, the scour depths at structure A do not represent maximum values.

Structure B shown in Fig. 8 is considered first. In the clear-water case (subfigures a and b), there was an observable asymmetry in scour development between the upstream and downstream piles of the jacket. At the downstream piles, the scour process had reached an equilibrium state, whereas at the upstream piles, scour was still developing after 420 min. A comparison to the scour development over time for combined wave-current conditions (Welzel et al., 2019a), the scour development

under current only conditions reveals larger differences in the local scour development between the upstream and downstream side of about $\Delta S/D = 0.47$ (comparing the maximum scour depth downstream and upstream). Despite clear-water conditions, the overall flow obstruction caused by the jacket impeded scour at the downstream piles.

Reference measurements taken with the E4 echosounder at a distance from the main piles indicate that no scour occurred under these conditions. The blocking effect of the structure at this location was therefore insufficient to accelerate or divert the flow to cause erosion.

Conversely, scour development on the downstream side (echosounder 8) initiated about 170 min after the beginning of the test. Looking at the scour pattern in Fig. 4, it is clear that this scour development is likely to be scour trails originating from the two upstream piles and reaching this location after approximately 170 min of the test. Thus the observed scour pattern does not represent global erosion due to flow constriction by the jacket structure. Rather, it is the effect and superposition of local scour around the upstream main piles.

In the live-bed case (subfigures c and d), the scour progression over time at the main piles was more consistent between the upstream and downstream piles. A asymmetry of about $\Delta S/D = 0.15$ between the maximum scour depth on the upstream and downstream side was measured. In contrast to the clear water case, significant erosion was measured at the reference locations (E4 and E8) from the beginning of the test under live-bed conditions, as expected. Here, the scouring process was more intense and more variable at the downstream reference location (E8) than at the upstream reference location (E4), which could be a further indication of the influence of local scour development at the upstream piles on the erosion process at this site. A comparison between the global scour development, highlighted with E4 and E8 and the linear regression (black dashed line) depicted in Fig. 8c and d with the local scour development around pile 1 and pile 3, reveals that the global scour progresses much slower at structure B as the local scour. No near equilibrium condition is observed for sensor E4 and E8 under live bed conditions at structure B.

Structure A shown in Fig. 9 is considered next. For the clear-water case, the almost linear scour development at all measurement points is immediately noticeable. However, this is probably due to the measurement positions being relatively far (3–4 cm) from the suction buckets and therefore not capturing the faster scour process at the beginning. It is also noticeable that the differences in scour depth between the reference measurements at positions E2 and E4 and the local scour measurements were very large. Similar to position E4 at the jacket, no scour could be measured at position E2. Given the clear-water conditions, the obstruction of the flow was not sufficient to generate local velocities above the critical value for sediment mobilisation. On the other hand, erosion occurs much earlier at position E4 than at position E8 under the jacket. However, position E4 in structure A is in the centre of the structure and not at the downstream end as position E8 at the jacket.

The development of scour under live-bed conditions is remarkable as the scour at the reference measurement points of E2 and E4 corresponds with the local scour development at each of the individual piles. As before, this indicates an early alignment of local scour development at the piles and global erosion in the center of the structure. This alignment is not observed for structure B, where the scour development at echosounders 4 and 8 differs significantly from that directly at the main piles.

4. Discussion

4.1. Remarks regarding scale effects and prototype comparison

The present study is affected by the well-known general problem of scaling sediment in laboratory experiments. Thus, the imbalance between scaled velocities and sediment grain size is likely to have resulted in an overprediction of bedload and an underprediction of suspended

sediment, potentially affecting the results and transferability of the present study. The flow dynamics across sediment ripples induces form drag and turbulence, leading to erosion on the stoss side (upstream) and sediment deposition on the lee side (downstream) of each ripple. The sediment ripples might therefore affect the boundary layer, possibly increasing in thickness and therefore also leading to larger horseshoe vortices, possibly influencing the scour development around the structures (Sumer and Fredsøe, 2002). According to Sutherland and Whitehouse (1998), the ripple migration in model scale also leads to a relatively increased sediment transport as in prototype scale with equal conditions. In chapter 3.3, a comparison of scour pattern surveys with in-situ field data of 4-legged jacket structures from four studies is presented, highlighting similarities and differences. To generally compare the results of the present study with field conditions, it's additionally essential to identify the temporal stage of the scouring process during the test, including whether an equilibrium stage has been reached or not, which has been analyzed and discussed in detail in chapter 3.4. Under field conditions the scour around the structure also undergoes additional effects as directional change of wave (Schendel et al., 2020) and current attack as well as refilling of the scour hole due to tidal currents (Schendel et al., 2019) or waves and seasonal aspects and changing storm conditions.

5. Summary and conclusion

Physical model tests were carried out to investigate the spatio-temporal scour development under current only flow conditions around two complex foundation structures, that significantly vary in their level of flow blockage. One structure is a novel hybrid gravity-based six-legged jacket (structure "A") with a comparable high flow blockage and the other a conventional four-legged jacket (structure "B") with a relative low flow blockage (a so called hydrodynamic transparent structure). In total 12 tests have been conducted (test 1a – 4c) under steady flow clear-water ($\bar{U} = 0.24$ m/s) and live bed ($\bar{U} = 0.42$ m/s) conditions. The bed topography was measured after each test accordingly with a 3D laser scanner, while the test duration was varied between 15, 90 and 420 min. Additionally, the scour development over time was measured with 8 mini echo sounder sensors, distributed strategically around the foundation structures.

- The time sequence of scour pattern and the temporal scour progression of the investigated structures reveals that global scour predominantly develops under live-bed conditions, regardless of the complexity or flow obstruction of the structure. This is assessed, as the spatially eroded sediment volume was calculated and transferred to a dimensionless representation enabling a comparison between both structures.
- No global scour was observed under clear-water conditions for both structure types over the test duration of 420 min. The normalized displaced sediment as well as the mean spatial distribution after 420 min is observed to be comparable (structure A: $\max -0.36 D_{i,i}$; structure B: $\max -0.37 D_{i,i}$) for both structures if normalized with the structure reference diameter as introduced with equation (1) and plotted over the normalized structure footprint.
- Under live bed conditions, a spatial erosion intensity was measured to be 2.5 times higher for structure A ($\max -2 D_{i,i}$) as for structure B ($\max -0.8 D_{i,i}$), indicating a nonproportional increase in erosion as the structural complexity and flow blockage increases, which also indicates a significant influence of complex structures with increased flow blockage on the surrounding marine environment.
- If compared to the scour development over time for combined wave-current conditions (Welzel et al., 2019a), the scour development under current only conditions reveals larger differences in the local scour development between the upstream and downstream side of about $\Delta S/D = 0.47$, while the differences are the largest under

clear-water conditions, live bed conditions reveal a asymmetry of about $\Delta S/D = 0.15$.

- A comparison of local and global scour at structure B under live bed conditions shows that global scour (E4 and E8) progresses significantly slower than the local scour at piles 1 and 3, potentially influencing further local scour development. Around structure An under live bed conditions, a merged scour develops. Scour at the reference positions E2 and E4 corresponds with the local scour development, indicating an early alignment of the local and global scour development and leading to similar scour depth and shape as observed for hexagonal cylinder arrays.
- The dimensionless comparison with in-situ field data of 4-legged jacket structures, generally confirms the spatial distribution and mean scour depth for the different time steps, measured in the present model tests. Thus highlighting that the present study might be a valuable tool to estimate the spatial extend and scour depths at common jacket structure designs, comparable with the utilized model. Furthermore the utilized dimensionless approach (also explained in Welzel, 2021) given by Eq. (1) not only allows a direct comparison of scour depths S/D and the spatial distribution, but enables also to calculate respective erosion volumes. Furthermore, the results enable to estimate which areas are exceeding a certain erosion threshold, also affecting the structure-induced morphological footprint in the marine environment.

CRediT authorship contribution statement

Mario Welzel: Writing – review & editing, Writing – original draft,

Visualization, Methodology, Investigation, Formal analysis, Conceptualization. **Alexander Schendel:** Writing – review & editing, Writing – original draft, Conceptualization. **Ramish Satari:** Writing – review & editing. **Insa Neuweiler:** Writing – review & editing, Supervision, Project administration, Funding acquisition. **Torsten Schlurmann:** Writing – review & editing, Supervision, Project administration, Funding acquisition.

Declaration of competing interest

The authors declare that they have no known competing financial interests or personal relationships that could have appeared to influence the work reported in this paper.

Data availability

Data will be made available on request.

Acknowledgements

This study has been carried out within the Collaborative Research Center (CRC) 1463 “Integrated design and operation methodology for offshore megastructures” and is funded by the Deutsche Forschungsgemeinschaft (DFG, German Research Foundation) – SFB 1463–434502799. As well as within the project TEXBASE (KF 3316902K14) which was funded by the ZIM program “Zentrales Innovationsprogramm Mittelstand” which is a funding programme of the BMWK (Federal Ministry for Economic Affairs and Climate Action).

Appendix A. – grain size distribution of the utilized sediment

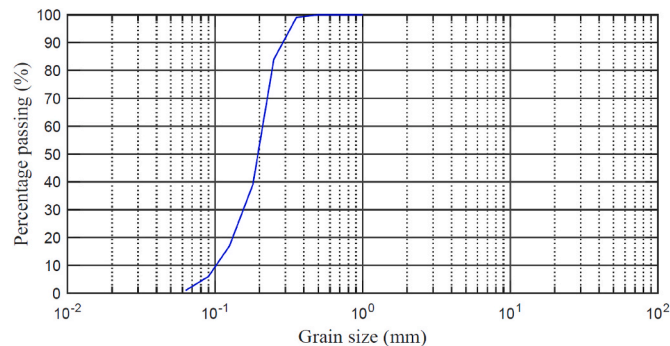


Fig. 10. Grain size distribution of the utilized sediment in the conducted model tests with $d_{50} = 0.19$ mm and a geometric standard deviation of $\sigma_s = \sqrt{d_{84}/d_{16}} = 1.4$.

Appendix B. – calculation of $D_{I,i}$ and field data calculation for Fig. 7

The dimensionless parameter $D_{I,i}$, see Eq. (1) utilizes the respective erosion or deposition volumes V_i of the sediment. These volumes V_i are calculated by subtracting a pre-scan topography of a post-scan topography of each test and subsequent calculation over the grid (see also Welzel et al., 2019b, 2020 for more details). Volumes V_i are always calculated for specific areas a_i . In Eq. (1), the respective volumes $V_i - V_{i-1}$ of increasing rectangular interrogation areas $a_i - a_{i-1}$ (see the highlighted area in) are divided by a representative sediment surface piercing structural diameter D (for structure A, $D = 13$ cm; for structure B, $D = 4$ cm).

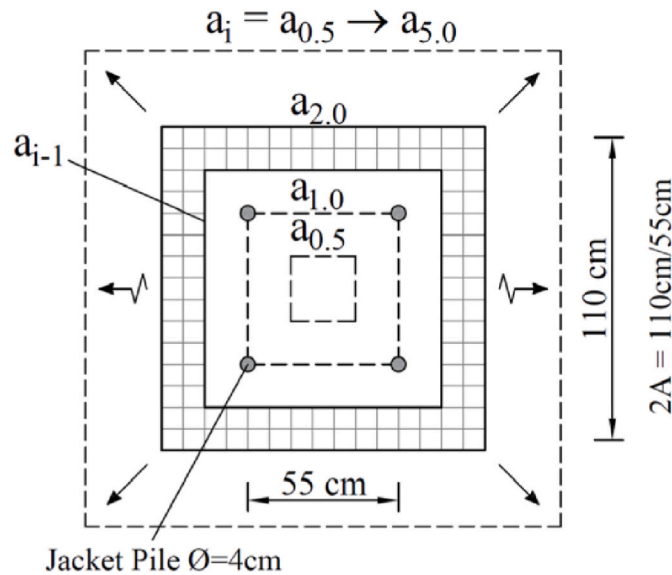


Fig. 11. Sketch of utilized interrogation areas a_i around the 4-legged jacket structure “B”, used to calculate volumes V_i . The area a_1 relates to the structure footprint area of the jacket model (0.55mx0.55m = 1A).

Thus the parameter $D_{l,i}$ is the same as the mean S/D value of a related area. Knowing the position and the area dimensions of the related parameter V_i , together with D, one can also easily calculate the respective volumes.

For Fig. 7, the topographic survey maps of each study (Harris and Whitehouse, 2021; Bolle et al., 2012; Baelus et al., 2019; Rudolph et al., 2004) are utilized to obtain representative S/D values for the same areas and distances (measured in reference to the structure footprint length A) from the center of the structure as used in Eq. (1) (see also above an). As the data are digitized with care over the illustrated topographies in each publication, the data might be affected with a small failure due to the digitization of the S/D values. Furthermore, the scour depths of are calculated in reference of post dredging surveys, prior of the installation for Bolle et al. (2012) and Baelus et al. (2019) as well as a reference height given in Rudolph et al. (2004). For Harris and Whitehouse (2021) we used the surrounding, uninfluenced seabed height (−18 m LAT).

Table 2
Field data of Fig. 7.

(1) S/D =	−0.25	−0.37	−0.17			
(2) S/D =	−0.19	−0.42	−0.11			
(3) S/D =	−0.28	−0.46	−0.20			
(4) S/D =	−0.87	−0.91	−0.68	−0.42	−0.16	−0.03
(5) S/D =	−0.95	−0.97	−0.65	−0.37	−0.21	
(x) A =	0.75	1.2	1.65	2.1	2.55	3.0

- (1) Harris and Whitehouse (2021).
- (2) Bolle et al. (2012); Jacket G2, 11/2011.
- (3) Bolle et al. (2012); Jacket G2, 01/2012.
- (4) Baelus et al. (2019); Jacket G2, 07/2013; D = .
- (5) Rudolph et al. (2004); D = 1.2 m.

References

Amini, A., Melville, B.W., Ali, T.M., Ghazali, A.H., 2012. Clear-water local scour around pile groups in shallow-water flow. *J. Hydraul. Eng.* 138 (2), 177–185. [https://doi.org/10.1061/\(ASCE\)HY.1943-7900.0000488](https://doi.org/10.1061/(ASCE)HY.1943-7900.0000488).

Baelus, L., Bolle, A., Szengel, V., 2019. Long term scour monitoring around offshore jacket foundations on a sandy seabed. In: *Proc. Of Ninth International Conference on Scour and Erosion (ICSE)*, Taipei, Taiwan, November 5.-8., 2018.

Beg, M., 2008. Effect of Mutual Interference of Bridge Piers on Local Scour. Ph.D. thesis, Department of Civil Engineering, Aligarh Muslim University, Aligarh, India.

Bolle, A., de Winter, J., Goossens, W., Haerens, P., Dewaele, G., 2012. Scour monitoring around o shore jackets and gravity based foundations. In: *Proceedings of the Sixth International Conference on Scour and Erosion, ICSE 6*, Paris, France, 27–31 August.

Breusers, H.N.C., 1972. *Local Scour Near Offshore Structures*, vol. 105. Delft Hydraulics Publication, Delft.

Chen, H., Zhang, J., Wang, F., Guo, Y., Guan, D., Feng, L., 2023. Experimental investigation of the current induced local scour around a jacket foundation. *Ocean Eng.* 285, 115369.

Ghods, H., Najafzadeh, M., Khanjani, M.J., Beheshti, A., 2021. Effects of different geometric parameters of complex bridge piers on maximum scour depth: experimental study. *J. Waterw. Port, Coast. Ocean Eng.* 147 (5), 04021021.

Gong, E., Chen, S., Chen, X., Guan, D., Zheng, J., 2023. Large-scale experimental study on scour around offshore monopile under combined wave and current condition. *Ocean Eng.* 283, 115186.

Harris, J.M., Whitehouse, R.J.S., 2021. Scour development around monopile and jacket foundations in Silty sands. In: *Proc. Of 10th International Conference on Scour and Erosion (ICSE)*, Arlington, Virginia, USA, October 18.-21.

Hirai, S., Kuruta, K., 1982. Scour Around Multiple- and Submerged Circular Cylinders, vol. 23. *Memoirs Faculty of Engineering, Osaka City University*, pp. 183–190.

Hosseini, R., Amini, A., 2015. Scour depth estimation methods around pile groups. *KSCSE J. Civ. Eng.* 19, 2144–2156. <https://doi.org/10.1007/s12205-015-0594-7>.

McGovern, D.J., Ilic, S., Folkard, A.M., McLelland, S.J., 2014. Time development of scour around a cylinder in simulated tidal currents. *J. Hydraul. Eng.* 140 (6).

Melville, B.W., Chiew, Y.M., 1999. Time scale for local scour in bridge piers. *J. Hydraul. Eng.* 125, 59–65.

Melville, B.W., Coleman, S.E., 2000. *Bridge Scour*. Water Resources Publication, CO.

Ni, X., Xue, L., 2020. Experimental investigation of scour prediction methods for offshore tripod and hexapod foundations. *J. Mar. Sci. Eng.* 8 (11), 856.

Rudolph, D., Bos, K.J., Luijendijk, A.P., Rietema, K., Out, J.M.M., 2004. Scour around offshore structures – analysis of field measurements. In: *Second International Conference on Scour and Erosion, ICSE 2*. 14.-17. November 2004 in Singapore.

Schandel, A., Welzel, M., Schlurmann, T., Hsu, T.-W., 2020. Scour around a monopile induced by directionally spread irregular waves in combination with oblique

- currents. *Coast Eng.* 161, 103751 <https://doi.org/10.1016/j.coastaleng.2020.103751>.
- Schendel, Alexander, Welzel, Mario, Arndt, Hildebrandt, Schlurmann, Torsten, Hsu, Tai-Wen, 2019. Role and impact of hydrograph shape on tidal current-induced scour in physical-modelling environments. *Water* 11 (12), 2636. <https://doi.org/10.3390/w11122636>.
- Sheppard, D.M., Odeh, M., Glasser, T., 2004. Large scale clear-water local pier scour experiments. *J. Hydraul. Eng.* 130, 957–963.
- Sheppard, D.M., Miller, W., 2006. Live-bed local pier scour experiments. *J. Hydraul. Eng.* 132 (7), 635–642.
- Soulsby, R., 1997. *Dynamics of Marine Sands: A Manual for Practical Applications*. Thomas Telford, London (UK).
- Soulsby, R., Clarke, S., 2005. Bed shear-stresses under combined waves and currents on smooth and rough beds. In: *Report TR 137 Rev 1.0 August 2005 HR Wallingford*.
- Sumer, B.M., Fredsøe, J., 2001. Scour around pile in combined waves and current. *J. Hydraul. Eng.* 127 (5), 403–411. [https://doi.org/10.1061/\(ASCE\)0733-9429\(2001\)127:5\(403\)](https://doi.org/10.1061/(ASCE)0733-9429(2001)127:5(403)).
- Sumer, B.M., Fredsøe, J., 2002. *The Mechanics of Scour in the Marine Environment*. World Scientific.
- Sumer, B.M., Bundgaard, K., Fredsøe, J., 2005. Global and local scour at pile groups. In: *Proc. 15th International Ocean and Polar Engineering Conference (ISOPE)*, Seoul, Korea.
- Sumner, D., 2010. Two circular cylinders in cross-flow: a review. *J. Fluid Struct.* 26 (6), 849–899. <https://doi.org/10.1016/j.jfluidstructs.2010.07.001>.
- Sutherland, J., Whitehouse, R.J.S., 1998. Scale Effects in the Physical Modelling of Seabed Scour. *Report TR 64; HR Wallingford, Wallingford, UK*.
- Welzel, M., Schendel, A., Hildebrandt, A., Schlurmann, T., 2019a. Scour development around a jacket structure in combined waves and current conditions compared to monopile foundations. *Coast Eng.* 152, 103515 <https://doi.org/10.1016/j.coastaleng.2019.103515>.
- Welzel, M., Schendel, A., Schlurmann, T., Hildebrandt, A., 2019b. Volume-based assessment of erosion patterns around a hydrodynamic transparent offshore structure. *Energies* 12, 3089. <https://doi.org/10.3390/en12163089>.
- Welzel, M., Schendel, A., Goseberg, N., Hildebrandt, A., Schlurmann, T., 2020. Influence of structural elements on the spatial sediment displacement around a jacket-type offshore foundation. *Water* 12 16, 1651. <https://doi.org/10.3390/w12061651>.
- Welzel, M., 2021. *Wave-current-induced Scouring Processes Around Complex Offshore Structures*. Ph.D. thesis, Gottfried Wilhelm Leibniz Universität, Hannover, Germany. <https://doi.org/10.15488/11225>.
- Welzel, M., Schendel, A., Satari, R., Hildebrandt, A., Neuweiler, I., Schlurmann, T., 2023. Sc. In: *Our Development Around Complex Offshore Foundations under Current Load in Proc. Of 11th International Conference on Scour and Erosion (ICSE)*, Copenhagen, Denmark, p. 2023.
- WindEurope, 2021. *Offshore wind in Europe: key trends and statistics 2020*. Tech. Rep. Wind Europe 2021.
- Xiao, Y., Jia, H., Guan, D., Liang, D., Yuan, S., Tang, H., 2021. Modeling clear-water scour around the high-rise structure foundations (HRSF) of offshore wind farms. *J. Coast Res.* 37 (4), 749–760. <https://www.jstor.org/stable/48640354>.
- Yagci, O., Yildirim, I., Celik, M.F., Kitsikoudis, V., Duran, Z., Kirca, V.O., 2017. Clear water scour around a finite array of cylinders. *Appl. Ocean Res.* 68, 114–129.